Available online at www.sciencedirect.com
ScienceDirect
Trans. Nonferrous Met. Soc. China 35(2025) 511−524
Transactions of Nonferrous Metals Society of China
www.tnmsc.cn

# Laser welding of molybdenum socket joint for ultra-high-temperature heat pipes based on niobium alloying

Jia-xuan ZHAO[1], Hong-da ZHANG[1], Lin-jie ZHANG[1], Xiang-dong DING[1], Yuan-jun SUN[1], Guang SUN[2]

1. State Key Laboratory for Mechanical Behavior of Materials, Xi'an Jiaotong University, Xi'an 710049, China;
2. China Nuclear Power Design Co., Ltd., Shenzhen 518172, China

Received 19 July 2023; accepted 8 April 2024

**Abstract:** The influence of Ti and Zr, Nb alloying on the microstructures and performance of laser-welded molybdenum socket joints was investigated. Following Nb alloying, the average microhardness of the fusion zone (FZ) increased from HV 194.7 to HV 283.3. Additionally, Nb can react with O to form dispersed $Nb_2O_5$ along grain boundaries, impeding grain boundary migration and dislocation movement while reducing the content of volatile Mo oxide along these boundaries. The incorporation of Nb in FZ partially inhibits pore defects and enhances joint load-bearing capacity. In comparison to the laser-welded joints without adding Nb (LW), the tensile strength of the laser-welded joints with Nb alloying (LW-Nb) was significantly improved by approximately 69% from 327.5 to 551.7 MPa. Furthermore, the fracture mechanism of the joints transitioned from intergranular fracture to transgranular fracture.
**Key words:** laser welding; molybdenum; heat pipe; niobium alloying; microstructure; performance

## 1 Introduction

In 1963, George Grover at the Los Alamos National Laboratory (LANL) developed a heat transfer element called a heat pipe. Heat pipes are passive heat exchanger elements that achieve heat transfer by relying on phase change and continuous circulation of internal working media [1−3]. Depending on the service temperature, heat pipes can be classified into room-temperature, medium-temperature, high-temperature, and ultra-high-temperature categories. Some of the heat pipes used in heat pipe reactors operate at temperatures above 1000 °C, making them ultra-high-temperature heat pipes. Additionally, the commonly used corrosive alkali metals for the working media in these systems include Li, Na, and K [1]. The harsh working environment necessitates careful material selection for producing effective heat pipes. Zirconium alloys are commonly chosen as cladding and heat pipe materials in nuclear reactors due to their excellent corrosion resistance and good mechanical properties. However, the oxidation behavior of zirconium alloys at extremely high temperatures remains a key issue for their long-term use. Although chromium coatings have been widely applied in past research to enhance the oxidation resistance of zirconium alloys, the degradation mechanism of chromium coatings, especially the peeling and embrittlement of the coating under high-temperature conditions, still limits their long-term use in high-temperature environments [4,5]. In contrast, molybdenum has better oxidation resistance than chromium, and its alloys possess higher melting points, smaller neutron absorption cross-sections, superior high-temperature performance, and excellent corrosion resistance to alkali metals, making it more suitable as a design material for heat pipes [6,7].

**Corresponding author:** Lin-jie ZHANG, Tel: +86-29-82663115, E-mail: zhanglinjie@mail.xjtu.edu.cn
DOI: https://doi.org/10.1016/S1003-6326(24)66696-3

Laser welding [8−11] offers several advantages compared to other welding methods, including not requiring a vacuum chamber, high energy density, low heat input during welding, small heat-affected zone (HAZ), and high machining efficiency. Consequently, laser welding is a welding method that holds great development potential for Mo alloys. However, Mo alloys still encounter several welding challenges, including the presence of pore defects and grain coarsening in both the fusion zone (FZ) and HAZ, which result in a reduction in their strength and toughness. Moreover, joint grain boundaries are susceptible to embrittlement, leading to increased propensity for crack formation. These issues significantly limit the practical application of Mo alloys in ultra-high temperature heat pipes.

To address these issues, scholars have also proposed various control measures to enhance the performance of joints, such as preheating prior to welding [12,13], laser remelting [14], and alloying techniques [15−17]. Among these approaches, further advancements can still be made in the field of alloying. Therefore, this study focuses on investigating the potential improvements in socket joint alloying for heat pipes. Alloying elements are generally shown in Mo matrix in two forms: forming solid solution with Mo or existing as the secondary phase. Common infinite solid solution elements in Mo include Ti, Nb, and W, while finite solid solution elements include Zr, Re, and Hf. With an excess of the finite solid solution elements, they may combine with Mo to form intermetallic compounds (IMCs) that decrease the performance of joints. Therefore, it is reliable to use infinite solid solution elements for alloying, which is also more widely studied. CHENG et al [15] explored influences of Ti on the microstructures and performance of laser-welded joints of Mo−30W alloys. By adding Ti, the tensile strength of laser-welded joints of Mo−30W alloys increases from 108.56 to 409.57 MPa, which reaches 58.34% that of the BM. $MoO_2$ and $WO_2$ phases are expulsed from grain boundaries in the weld of Mo−30W joints without Ti, which significantly decreases the strength of grain boundaries and leads to a very low tensile strength. After adding Ti, $TiO_2$ phases are formed at grain boundaries, which reduce the amounts of $MoO_2$ and $WO_2$ phases that are harmful for the strength of grain boundaries and thus weaken the embrittlement trend of grain boundaries. ZHANG et al [16,17] explored the microstructure evolution and embrittlement of EBW joints of TZM alloys and the improvement mechanism of rhenium (Re) interlayers on microstructures and performance of joints. The previous research results show that serious grain coarsening happens in the FZ of joints without adding alloying elements, and $MoO_2$ and $TiO_2$ are segregated at grain boundaries, which results in the reduction of tensile strength of joints. The joints show intergranular fractures.

The alloying elements selected for welding of Mo alloys should exhibit slight deviations in physico-chemical properties compared to the BM, possess a significant solid solubility in the BM, and demonstrate strong affinity towards oxygen binding. Mo and Nb differ slightly in physico-chemical properties, have approximate melting points, and the generated solid solution has a high melting point. In addition, they are infinitely mutually soluble and have favorable metallurgical compatibility. By referring to the manual of thermodynamics [18], the reaction equations and Gibbs functions for standard molar reactions of Mo−O, Nb−O, Zr−O, and Ti−O were obtained, and the corresponding O-potential diagrams were drawn, as shown in Fig. 1(a). It can be seen from Fig. 1(a) that $Nb_2O_5$ is located at the lowest on the O-potential diagram. Theoretically, Nb is of higher affinity with O and therefore the generated oxides are more stable. The melting points of $MoO_2$, $NbO_2$, and $Nb_2O_5$ are separately 2300, 1900, and 1520 °C, respectively. Comparison shows that Nb oxides have lower melting points and therefore may be expulsed from grain boundaries in the solidification process, thus inhibiting the formation and segregation of $MoO_2$ phases at grain boundaries and playing a role in purifying grain boundaries.

According to the phase diagram of Mo−Nb (Fig. 1(b)), considering the compatibility of physico-chemical properties and analysis of the O-potential diagram, Nb is considered an optimal alloying element for welding Mo heat pipes, exhibiting potential in enhancing high-temperature performance of welded joints in Mo heat pipes. Based on this premise, in this study the influence of incorporating a small amount of Nb on defects, microstructures, and mechanical properties of joints was systematically investigated. The laser-welded Mo tube-end plug socket joints of Mo heat pipes were chosen as the subjects of this research.

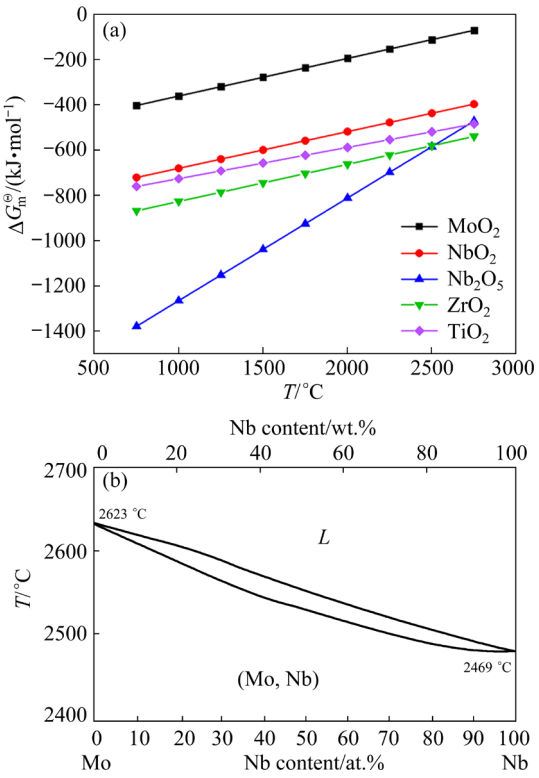


**Fig. 1** Feasibility analysis results of Nb as alloying element for Mo fusion welding: (a) O-potential diagram for Mo−O, Nb−O, Zr−O, and Ti−O; (b) Mo−Nb phase diagram

## 2 Experimental

### 2.1 Materials

The experimental materials used in this study were pure Mo end plug and $La_2O_3$ dispersion-strengthened Mo alloy tube in which the content of La was about 0.25 wt.%. The alloying material was RO4200 Nb foil with a thickness of 0.1 mm and a Nb content of 99.95 wt.%, which was machined into a Nb ring with the outer diameter of 16 mm and inner diameter of 14.4 mm (Fig. 2(a)). For the convenience of comparison, two types of joints were prepared: laser-welded joints without alloying (LW joint) and laser-welded joints with Nb alloying (LW-Nb joint). The assembly of the two types of joints and the adding scheme of Nb foil are displayed in Figs. 2(b) and (c) [19].

### 2.2 Methods

The laser welding system consisted of an IPG YLS−8000 fiber laser, an ABB robot, a rotating fixture, and an argon shield apparatus. The laser operated at a maximum output power of 8 kW, with a focal spot diameter of 200 μm, a wavelength of 1068 nm, and a focal length of 200 mm. The welding setup and orientation are depicted in Fig. 3. The welding parameters were configured as follows: laser power 2200 W, defocusing amount 0 mm, welding time 4.5 s, and remelting cycles 8.

Before the welding experiments, the Mo tube and end plug underwent initial treatment by grinding with abrasive paper to remove the oxide layer. They were then ultrasonically cleaned in acetone before being dried and assembled. A rotating fixture was used to secure the Mo tube−end plug component during welding; as shown in Fig. 3, the interface between the Mo tube and end plug

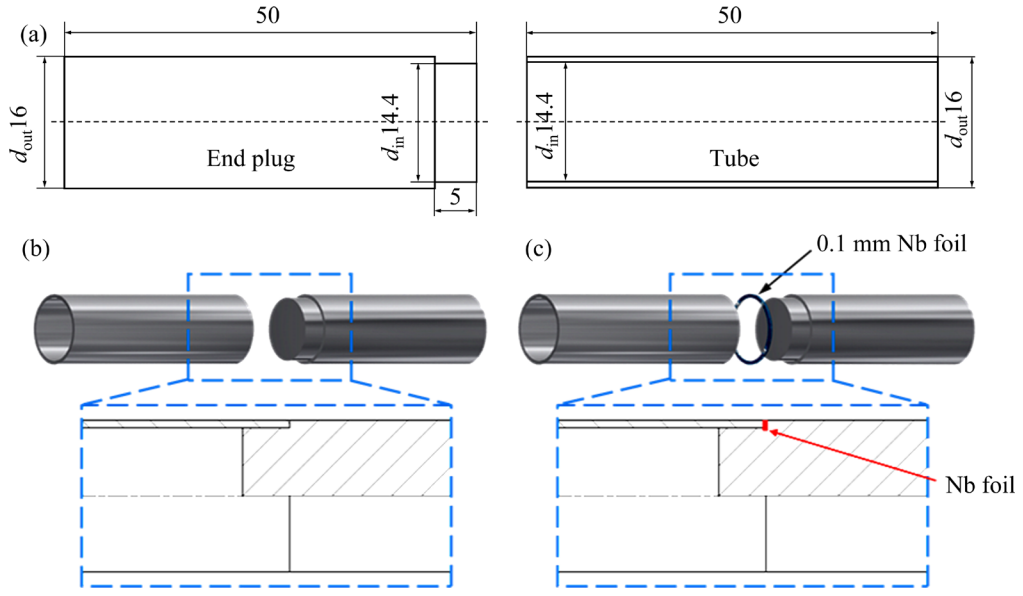


**Fig. 2** Assembly of two joints and adding scheme of Nb foil: (a) Dimensions of pure Mo tubes and end plug; (b) LW joint; (c) LW-Nb joint (Unit: mm)

served as the location for welding. Argon gas was introduced into the shielding system during the welding process. To preheat the Mo tube−end plug component to 600 °C, a heater coil was utilized. During welding operations, while keeping the laser head stationary, the workpiece rotated continuously. Post-welding, the workpiece was naturally cooled down below 100 °C in the argon gas shield environment.

The cross-sectional metallographic samples of the joints were prepared and the etchant was a mixed solution of 15% $K_3[Fe(CN)_6]$ solution and 15% NaOH solution with the volume ratio of 2:1. The cross-sectional metallographic structures were observed using a Nikon Eclipse MA200 optical microscope. An SU8230 cold field scanning electron microscope (SEM) with the energy dispersive spectrum (EDS) system thereon was used to analyze the cross-sectional morphologies, element composition and distribution, and micro-morphologies of tensile fractures of the joints. An Oxford EBSD system was adopted to analyze crystal preferred orientation, phase compositions and distribution in the FZ and HAZ on cross sections of the joints. Additionally, an Xradia 610 Versa X-ray imager was utilized for nondestructive inspection of pore defects in welds. The Vickers microhardness testing was performed using an SCTMC XHVT−1000Z Vickers hardness tester with a load of 2 N for 10 s. Room-temperature tensile tests were conducted on an INSTRON universal testing machine.

## 3 Results

### 3.1 Microstructures and compositions

Figure 4 compares the macro-morphologies of welds and cross-sectional metallographic structures of the LW and LW-Nb joints. Both welds exhibit a gleaming silver-white metallic luster without any visible cracks or surface splatters. The FZs of both joints display an inverted-cone morphology. The weld width and penetration of the LW joint are 0.87 and 1.39 mm, respectively, while those of the LW-Nb joint are 0.90 and 1.35 mm, respectively. It is apparent that the two joints have similar weld width and penetration, likely due to the comparable physico-chemical properties of Mo and Nb. The FZs of both joints consist of columnar grains growing towards the center of the weld, with lambdoid grains in the upper part of the welds. The HAZs of both joints exhibit recrystallized microstructures that have coarsened after thermal cycles during welding.

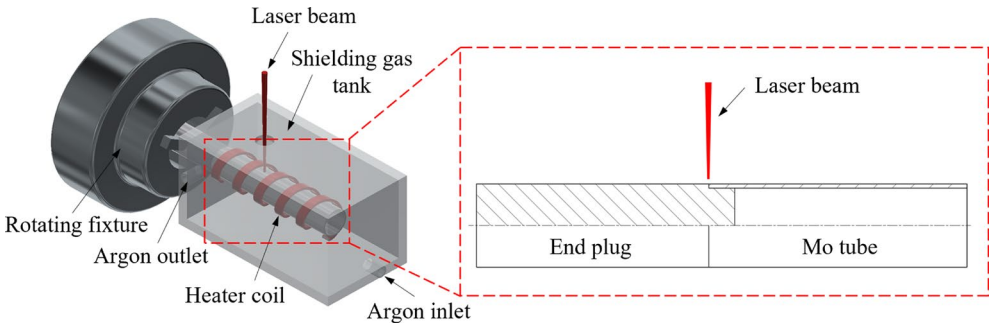


**Fig. 3** Schematic diagram for welding fixture and welding position

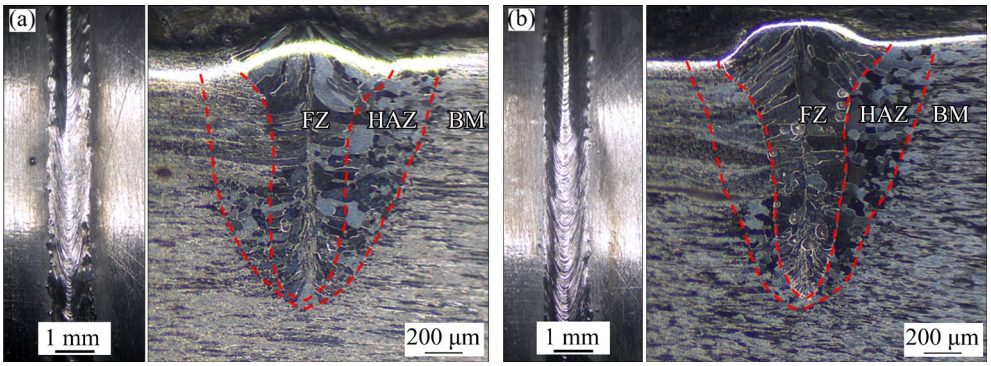


**Fig. 4** Macro-morphologies of welds and metallographic structures of two joints: (a) LW joint; (b) LW-Nb joint

The EDS scanning results in Fig. 5 show the distribution of elements on the cross-sections of the two joints. The EDS mapping results of the LW-Nb joint (Fig. 5(b)) reveal that Nb is uniformly distributed in the FZ without any macroscopic segregation. The EDS point scanning results (Tables 1 and 2) show that the O contents in the FZ of the LW joint and LW-Nb joint are 3.78 wt.% and 2.26 wt.%, respectively, suggesting that Nb alloying helps in reducing the O content in the FZ. The Nb content in the FZ of the LW-Nb joint accounts for about 10 wt.%. Based on the Mo−Nb binary phase diagram, the melting point of the Mo−10Nb solid solution changes between 2600 and 2620 °C, indicating minimal deviation from that of the Mo matrix, ensuring the high-temperature performance of weld.

**Table 1** EDS point scanning results of cross-sections of LW joint

| Test No. | Element content/wt.% | | Total/wt.% |
|---|---|---|---|
| | Mo | O | |
| 1 | 96.75 | 3.25 | 100 |
| 2 | 98.49 | 1.51 | 100 |
| 3 | 95.79 | 4.21 | 100 |
| 4 | 96.73 | 3.27 | 100 |
| 5 | 96.56 | 3.44 | 100 |
| 6 | 93.01 | 6.99 | 100 |
| Average | 96.22 | 3.78 | 100 |

**Table 2** EDS point scanning results of cross-sections of LW-Nb joint

| Test No. | Element content/wt.% | | | Total/wt.% |
|---|---|---|---|---|
| | Mo | Nb | O | |
| 1 | 88.52 | 9.64 | 1.84 | 100 |
| 2 | 87.00 | 10.27 | 2.73 | 100 |
| 3 | 87.21 | 10.39 | 2.40 | 100 |
| 4 | 87.64 | 10.44 | 1.92 | 100 |
| 5 | 88.51 | 8.98 | 2.51 | 100 |
| 6 | 87.81 | 10.06 | 2.13 | 100 |
| Average | 87.78 | 9.96 | 2.26 | 100 |

### 3.2 Microhardness distribution and tensile performance

The microhardness distribution across the cross-sections of the two joints is illustrated in Fig. 6 and Table 3. It is evident that the average microhardness of the FZ in the LW joint is lower than that of the BM, whereas the average microhardness of the FZ in the LW-Nb joint is higher than that of the BM. Specifically, the FZ in the LW-Nb joint exhibits an average microhardness of HV 283.3, significantly surpassing that of HV 194.7 for the FZ in the LW joint. This variance can be attributed to the solid solution strengthening effect of Nb. Furthermore, the HAZs in both joints experience processes of recovery, recrystallization, and grain growth after the thermal cycles occur during welding at elevated peak temperatures. Consequently, the work hardening of the BM following

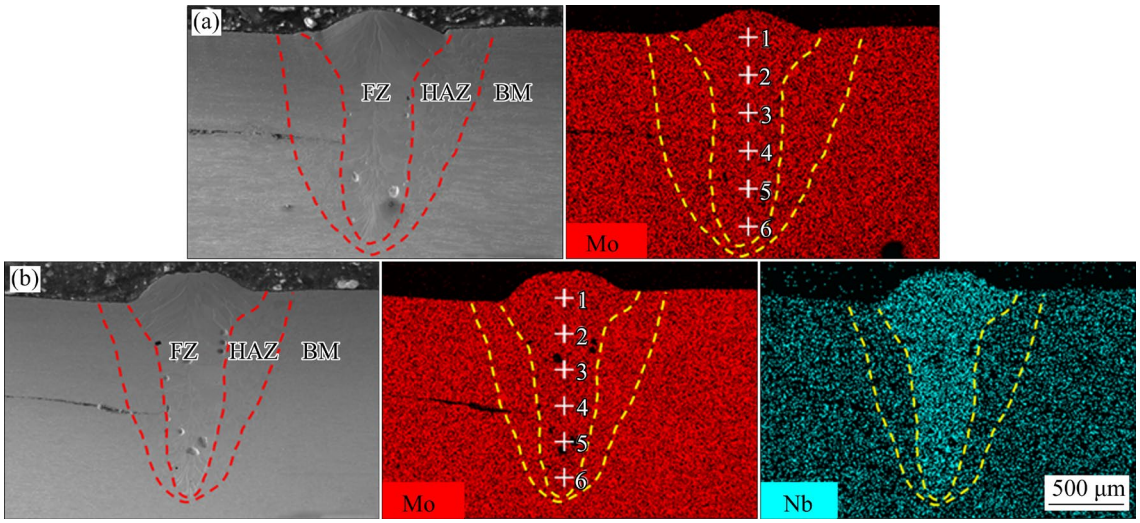


**Fig. 5** EDS mapping scanning and point scanning positions for element distribution on cross-sections of two joints: (a) LW joint; (b) LW-Nb joint

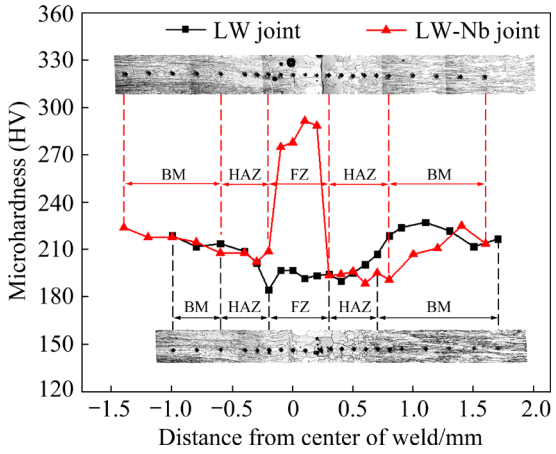


**Fig. 6** Microhardness distribution curves of two joints

**Table 3** Distribution of average microhardness of two joints

| Welded joint | Average hardness (HV) | | | | |
|---|---|---|---|---|---|
| | BM of Mo tube | HAZ of Mo tube | FZ | HAZ of end plug | BM of end plug |
| LW | 214.8 | 198.2 | 194.7 | 198.2 | 220.1 |
| LW-Nb | 218.6 | 206.8 | 283.3 | 193.1 | 214.2 |

cold forming diminishes, leading to a reduction in the number of grain boundaries and consequent softening of the HAZs in the joints.

The results of the room-temperature tensile test for the two joints are shown in Fig. 7, indicating that the LW and LW-Nb joints have tensile strengths of 327.5 and 551.7 MPa, respectively. This indicates a significant increase in strength due to Nb alloying. Both joints experienced brittle fractures at the weld site. Close-up views of the tensile fractures for the LW and LW-Nb joints are shown in Figs. 8 and 9, respectively. The fracture morphology of the LW joint mainly consisted of intergranular fractures with sporadic cleavage fractures. In contrast, the LW-Nb joint exhibited primarily cleavage fractures with some intergranular fractures. It is evident from Fig. 9(f) that the wall thickness at the fracture location is smaller compared to other areas, implying

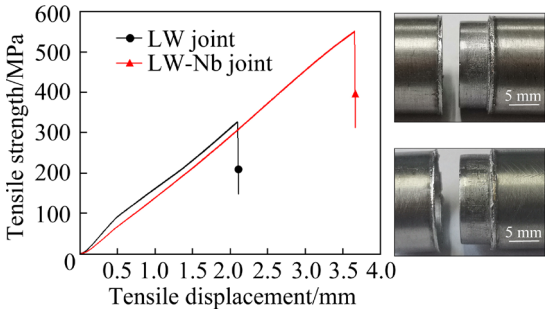


**Fig. 7** Tensile test results of two joints

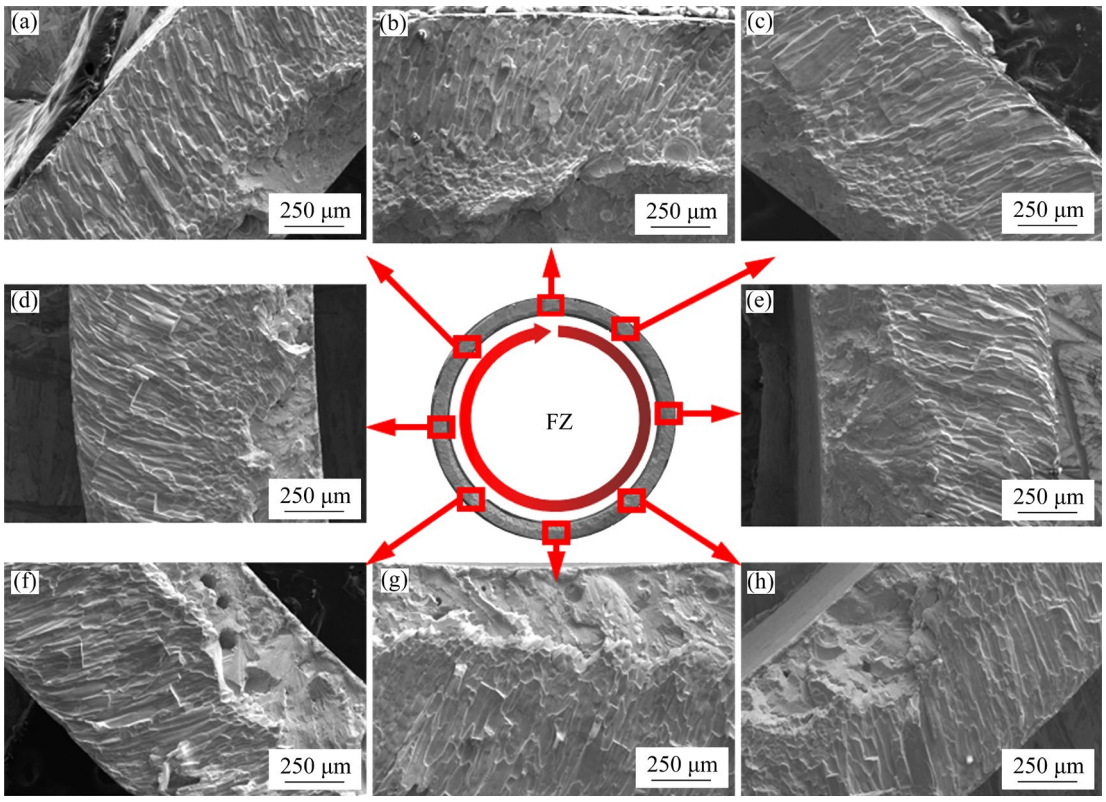


**Fig. 8** Close-up views of tensile fracture of LW joint

that this area is not located at the center of the weld. The observation of pores in Fig. 9(f) suggests that the fracture occurred near the fusion line.

Figures 10 and 11 provide close-up views of the tensile fractures of the LW and LW-Nb joints, respectively. In the fracture of the LW joint, coarse columnar grains are visible near the outer wall of the tube, while river patterns consisting of a mix of equiaxed grains and cleavage steps can be observed near the inner wall. Figure 10 also reveals pore defects in the region adjacent to the tube inner wall in the LW joint fracture. On the other hand,

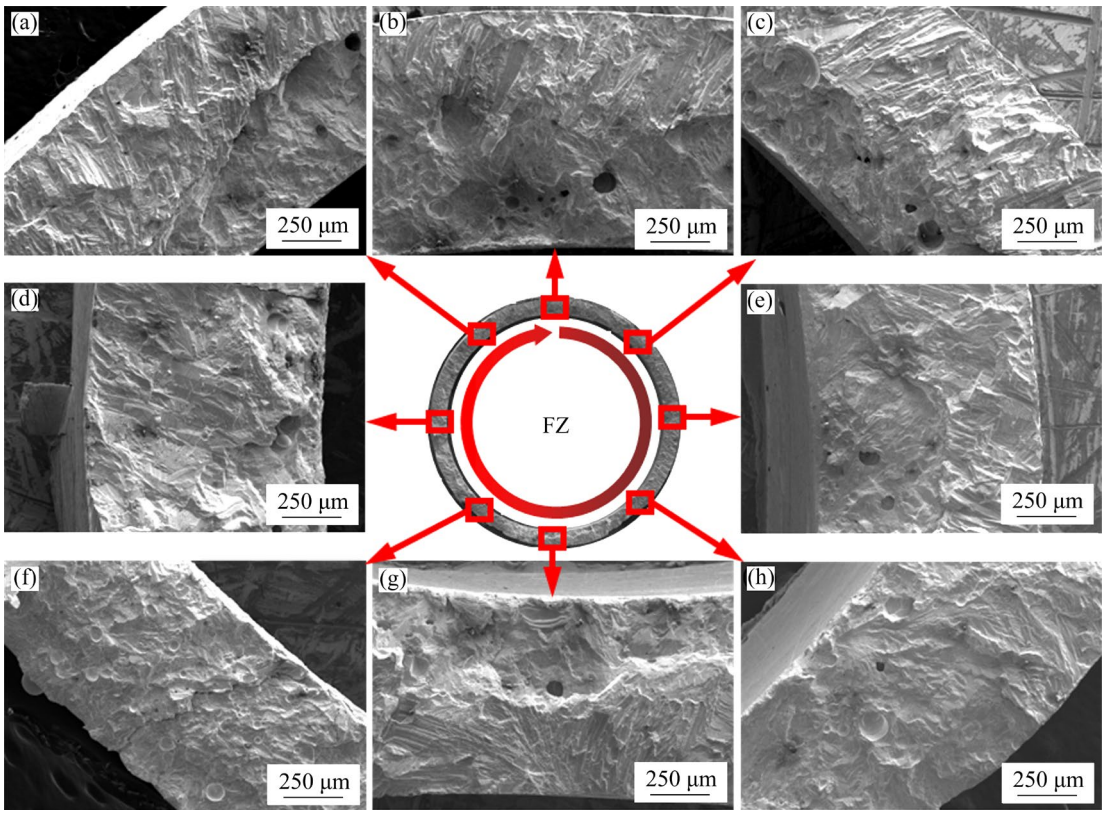


**Fig. 9** Close-up views of tensile fracture of LW-Nb joint

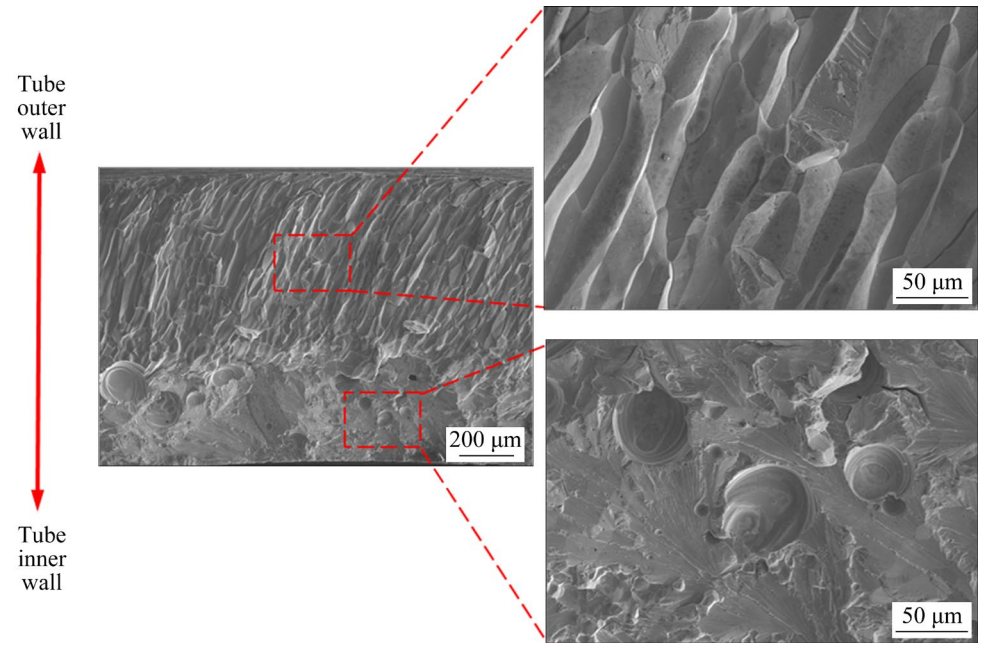


**Fig. 10** Local morphologies of tensile fracture of LW joint

predominantly cleavage fractures are displayed in the fracture of LW-Nb joint, with more irregular and smaller-sized cleavage steps near its inner wall compared to those near its outer wall. Figure 11 illustrates that numerous pore defects are also present in this tensile fracture near its inner wall.

The morphologies of the tensile fracture of the LW joint at high magnification are shown in Fig. 12. Pyramidal, lamellar, and dot-chain-shaped precipitated phases are distributed on the surface of grain boundaries, as illustrated in Figs. 12($b_2$) and ($c_2$). EDS point scanning of the precipitated phases shown in Fig. 12($b_2$), displayed in Table 4, indicates a higher oxygen content compared to the matrix, suggesting the presence of Mo oxides.

The morphologies of the tensile fracture of the LW-Nb joint at high magnification are depicted in Fig. 13. In Figs. 13($b_1$) and ($b_2$), numerous tiny globular bright white precipitated phases are dispersed on the surface of grain boundaries. EDS point scanning of the precipitated phases (Table 5) in Fig. 13($b_2$) reveals an increase in both Nb and O contents, while the Mo content decreases in the precipitated phases at grain boundaries in the LW-Nb joint fracture as compared to those in the LW joint fracture, indicating the presence of Nb oxides. The Nb oxides compete with Mo for O, thereby reducing the expulsion of Mo oxides at grain boundaries. Additionally, the dispersed Nb oxides hinder the movement of grain boundaries

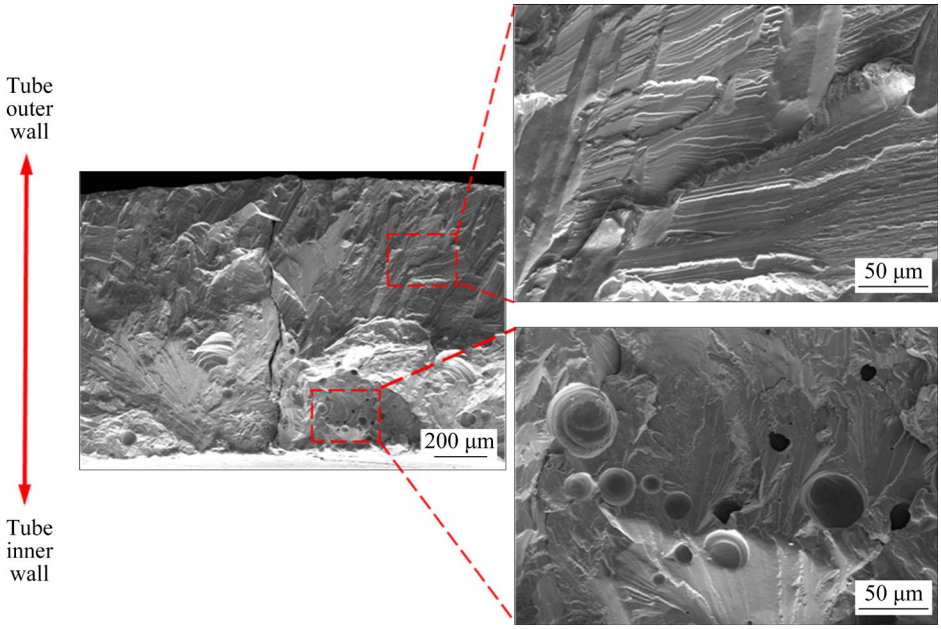


**Fig. 11** Local morphologies of tensile fracture of LW-Nb joint

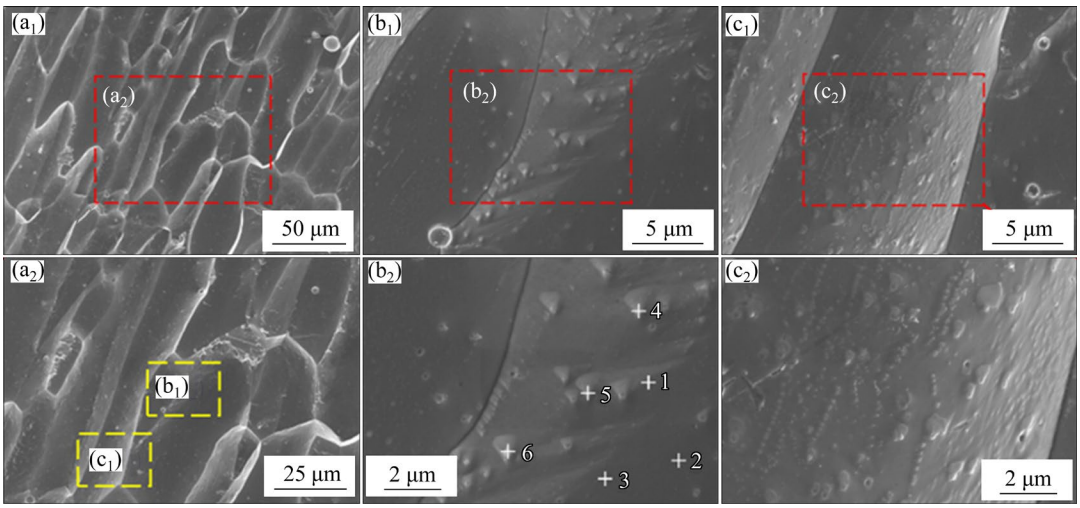


**Fig. 12** Morphologies of tensile fracture of LW joint at high magnification and EDS point scanning positions of secondary phase

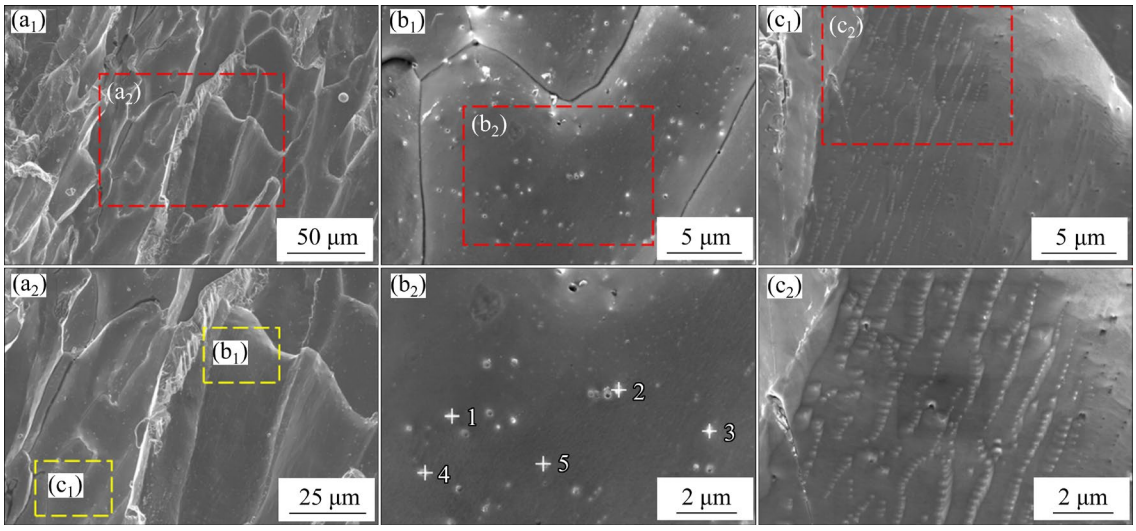


**Fig. 13** Morphologies of tensile fracture of LW-Nb joint at high magnification and EDS point scanning positions of secondary phase

**Table 4** EDS point scanning results of secondary phase in tensile fracture of LW joint

| Point in Fig. 12($b_2$) | Element content/at.% | | Total content/at.% |
|---|---|---|---|
| | Mo | O | |
| 1 | 100.00 | 0 | 100 |
| 2 | 99.25 | 0.75 | 100 |
| 3 | 99.49 | 0.51 | 100 |
| 4 | 96.27 | 3.73 | 100 |
| 5 | 96.05 | 3.95 | 100 |
| 6 | 96.67 | 3.33 | 100 |

**Table 5** EDS point scanning results of secondary phase in tensile fracture of LW-Nb joint

| Point in Fig. 13($b_2$) | Element content/at.% | | | Total content/at.% |
|---|---|---|---|---|
| | Mo | Nb | O | |
| 1 | 41.08 | 6.47 | 52.45 | 100 |
| 2 | 44.02 | 4.54 | 51.44 | 100 |
| 3 | 48.82 | 7.03 | 44.15 | 100 |
| 4 | 50.43 | 5.17 | 44.40 | 100 |
| 5 | 42.75 | 5.28 | 51.97 | 100 |

and dislocations, collectively contributing to the strength enhancement of grain boundaries and joints. Furthermore, dot-chain-shaped precipitated phases similar to those observed in the LW joint fracture are also shown at grain boundaries in the fracture of the LW-Nb joint, as seen in Figs. 13($c_1$) and ($c_2$).

## 4 Discussion

### 4.1 Grain size

The grain sizes in the FZs of both joints were statistically analyzed using the streaking method, with the statistical region highlighted within the yellow box in Fig. 14. The average grain size for the LW joint is 36.5 μm, while that for the LW-Nb joint is 35.2 μm. This suggests that Nb alloying does not have a significant refining effect on grains in the FZ.

### 4.2 Phase constitution of joints

Electron backscattering diffraction (EBSD) measurement was used to analyze the FZs of both joints. The phase distribution is shown in Fig. 15, and the statistical results of the relative phase contents are listed in Table 6. In the FZ of the LW joint, the identified phases consist of Mo, $MoO_2$, and $MoO_3$, while in the FZ of the LW-Nb joint, Mo, $MoO_2$, $MoO_3$, and $Nb_2O_5$ are detected. The addition of Nb leads to a reduction in the content of Mo oxides and the formation of $Nb_2O_5$ phases. In Fig. 15(a), most Mo oxides in the LW joint are dispersed sporadically along the grain boundaries, with some forming clustered chains, thereby diminishing bond strength and increasing brittleness at the grain boundaries. In contrast, in Fig. 15(b), $Nb_2O_5$ phases in the FZ of the LW-Nb joint are dispersed sporadically along the grain boundaries, enhancing both grain boundary and joint strengths.

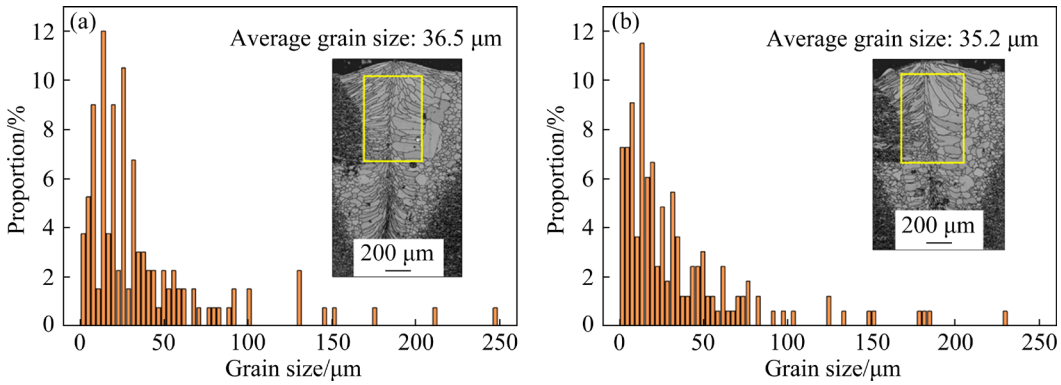


**Fig. 14** Grain size distribution in FZs of two joints: (a) LW joint; (b) LW-Nb joint

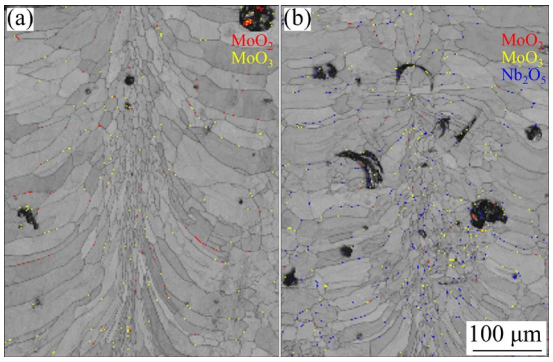


**Fig. 15** Phase distribution in FZs of two joints: (a) LW joint; (b) LW-Nb joint

**Table 6** Relative contents of different phases in FZs of two joints (%)

| Welded joint | Relative content/% | | | | | Rate of no resolution/% |
|---|---|---|---|---|---|---|
| | Mo | $MoO_2$ | $MoO_3$ | $Nb_2O_5$ | $NbO_2$ | |
| LW | 98.21 | 0.09 | 0.23 | – | – | 1.47 |
| LW-Nb | 97.72 | 0.06 | 0.24 | 0.38 | – | 1.60 |

Consequently, Nb exists in the weld in two forms: one dissolving in the matrix for solid solution strengthening, and the other reacting with O to produce oxides (second-phase particles) that are distributed along the grain boundaries, contributing to dispersion strengthening and purifying the grain boundaries.

### 4.3 Types of grain boundaries

EBSD was utilized to analyze the high-angle grain boundaries (HAGBs) and low-angle grain boundaries (LAGBs) in the FZs of the two joints, with their distribution displayed in Fig. 16. The yellow boxes in Fig. 16 highlight the joint bearing areas, where significantly more LAGBs were observed in the LW-Nb joint compared to the LW joint. Since the interfacial energy of LAGBs is lower than that of HAGBs, and reducing the interfacial energy of grain boundaries can enhance the strength of grain boundaries to some extent, Nb alloying could improve the joint strength by influencing the types and interfacial energy of grain boundaries.

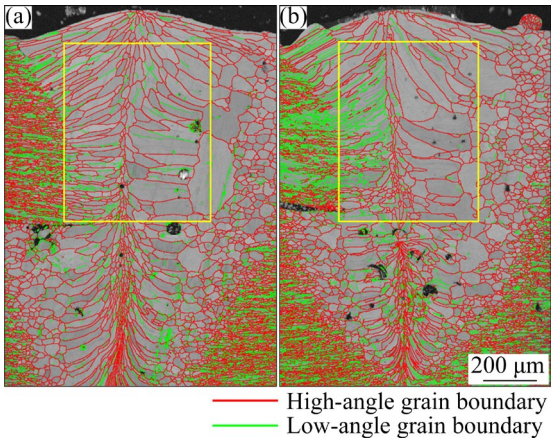


**Fig. 16** Distribution of HAGBs and LAGBs in FZs of two joints: (a) LW joint; (b) LW-Nb joint

### 4.4 Pore defects

Disc samples, with 1.5 mm in thickness, were extracted from the welds of the two joints for CT inspection. Statistical analysis of the distribution, number, and size of pore defects was conducted using Dragonfly software. The distribution of pore defects in both joints is illustrated in Fig. 17. The welds in both joints exhibit numerous pore defects, with small round pores spread throughout the welds and larger irregular pores mainly located at the bottom of the welds. A total of 668 pores with diameters ranging from 26 to 756 μm were

identified in the LW joint. In the LW-Nb joint, 600 pores with diameters ranging from 26 to 522 μm were detected. A comparison between the LW joint and the LW-Nb joint revealed a reduction of 10% in the number of pores and a decrease of 31% in the maximum pore diameter. The software's resolution limit for pore recognition was consistent due to the similar size of the two joints, and the minimum pore diameter was set to be 26 μm in both cases.

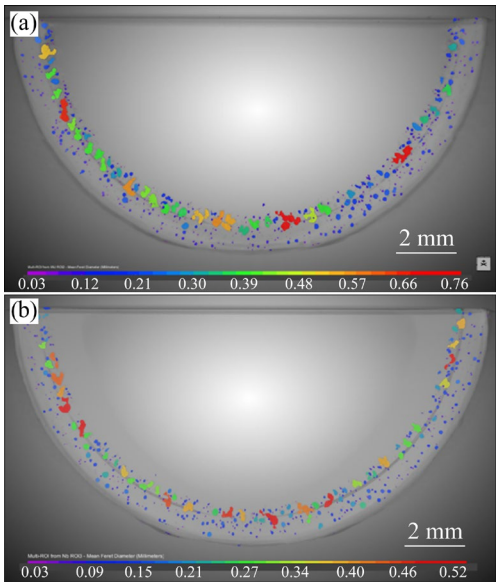


**Fig. 17** Cloud pictures showing distribution of pore defects in two joints: (a) LW joint; (b) LW-Nb joint

Figure 18 displays the statistical results of pore defect size distribution in both joints. It is evident that both joints exhibit a similar distribution of pore defects across a range of sizes, primarily falling within the range of 0−100 μm. However, the LW joint shows a higher occurrence of larger pores compared to the LW-Nb joint.

The EDS point scanning results of pore defects on the fractures of the two joints are displayed in Fig. 19. Tables 7 and 8 show the EDS point scanning results for the tensile fracture of two different joint types, respectively. It is worth noting that the pore defects in both joints exhibit a higher oxygen content compared to the matrix. The LW-Nb joint demonstrates a lower oxygen content in its pore defects than the LW joint, attributed to strong affinity of Nb for oxygen.

ZHANG et al [20] discovered that Zr alloying significantly reduces pore defects in laser-welded Mo joints by potentially inhibiting the formation

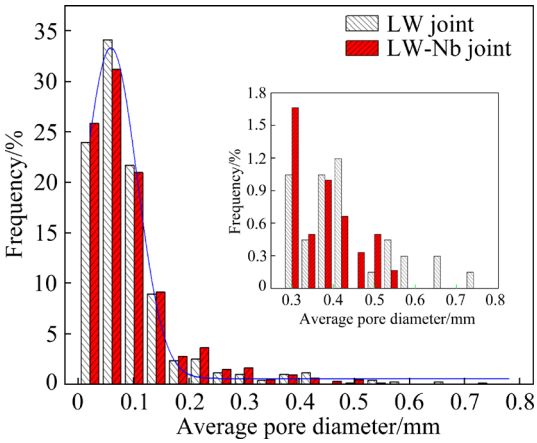


**Fig. 18** Statistical results for size distribution of pore defects in two joints

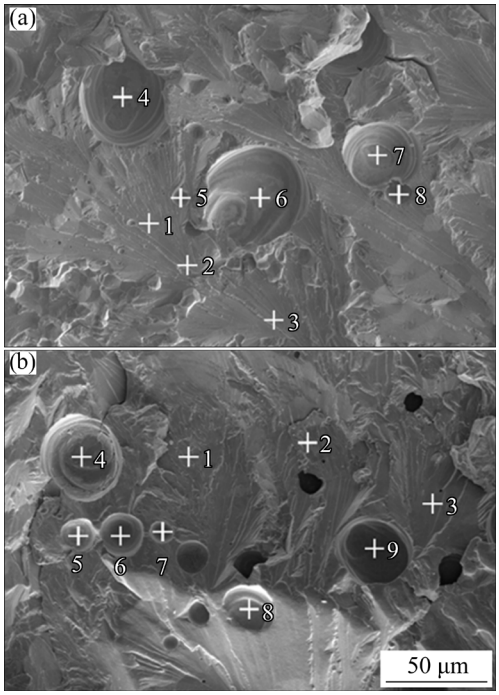


**Fig. 19** Morphologies of pores in tensile fractures of two joints and EDS point scanning positions: (a) LW joint; (b) LW-Nb joint

of low-boiling-point Mo oxides through the combination of Zr and O. Figure 1(a) illustrates that Nb has a greater tendency to combine with O compared to Zr. However, the influence of Nb alloying on pore defects in Mo welds is not pronounced, as evidenced by Fig. 17. This observation indicates that the generation mechanism of pore defects in laser-welded Mo joints is intricate and likely involves multiple mechanisms. Furthermore, the metallographic structures depicted in Fig. 4 reveal the distribution

**Table 7** EDS point scanning results of tensile fracture in LW joint

| Point in Fig. 19(a) | Element content/wt.% | | Total content/wt.% |
|---|---|---|---|
| | Mo | O | |
| 1 | 98.56 | 1.44 | 100 |
| 2 | 98.98 | 1.02 | 100 |
| 3 | 99.11 | 0.89 | 100 |
| 4 | 80.47 | 19.53 | 100 |
| 5 | 92.07 | 7.93 | 100 |
| 6 | 67.98 | 32.02 | 100 |
| 7 | 76.38 | 23.62 | 100 |
| 8 | 88.78 | 11.22 | 100 |

**Table 8** EDS point scanning results of tensile fracture in LW-Nb joint

| Point in Fig. 19(b) | Element content/wt.% | | | Total content/wt.% |
|---|---|---|---|---|
| | Mo | Nb | O | |
| 1 | 88.77 | 10.23 | 1.00 | 100 |
| 2 | 87.66 | 11.13 | 1.21 | 100 |
| 3 | 88.41 | 10.23 | 1.36 | 100 |
| 4 | 69.06 | 7.65 | 23.29 | 100 |
| 5 | 85.56 | 10.95 | 3.49 | 100 |
| 6 | 83.79 | 11.32 | 4.89 | 100 |
| 7 | 83.33 | 10.18 | 6.49 | 100 |
| 8 | 88.28 | 9.70 | 2.02 | 100 |
| 9 | 86.80 | 9.84 | 3.36 | 100 |

of specific pore defects around the fusion line primarily attributable to: (1) sealed micro-pores present in the base material of powder metallurgy materials, causing bubbles from incompletely fused micro-pores near the fusion line to be absorbed into the mushy zone at the solid−liquid interface and unable to escape; (2) flowing bubbles moving towards highly viscous mushy zone at the solid−liquid interface where they become trapped; (3) potential for gaps between grain boundaries at solidification front acting as a source of resistance for floating bubbles.

The analysis of the experimental phenomena above sheds light on the reasons behind pore defect formation, offering a novel approach for future research aimed at improving laser welding of ultra-high-temperature heat pipes. Decreasing the oxygen content in the molten pool during welding can reduce the likelihood of weld porosity formation. Introducing a gas in the shielding atmosphere that can chemically react with oxygen may be a beneficial strategy to mitigate pore defects. Additionally, increasing the number of remelting cycles during welding can facilitate bubble escape from the molten pool, consequently reducing pore defect formation in welded joints.

The above findings indicate that the inclusion of Nb alloy moderately reduces both the quantity and size of pore defects without significantly affecting their distribution. In general, Nb alloying partially hinders the occurrence of pore defects and helps the improvement of the joint strength.

Compared to the research findings of ZHANG et al [21], Nb alloying does not show a significant inhibitory effect on pore defects. This can be explained by two main factors: (1) Both the solidification rate and viscosity of the molten pool impact bubble release. Nb has a melting point (2469 °C) close to that of Mo (2620 °C), while the melting point of Zr is considerably lower. Under the same heat input conditions, Nb alloying results in a faster solidification rate and higher molten pool viscosity compared to Zr alloying, affecting bubble release. (2) When the temperature exceeds 2750 °C, $Nb_2O_5$ has a higher Gibbs free energy change than $ZrO_2$, indicating that Zr has a stronger affinity for oxygen than Nb. The Gibbs free energy change level in the O-potential diagram reflects the oxygen affinity of alloying element, but not the exact amount of oxygen involved in the reaction. Further investigation based on equilibrium constants is necessary to determine the extent of this reaction.

## 5 Conclusions

(1) After Nb alloying, the main phases observed are Mo, $MoO_2$, $MoO_3$, and $Nb_2O_5$, the content of Mo oxides declines, and Nb competes with Mo for O to form $Nb_2O_5$ that is dispersed at grain boundaries. Nb alloying reduces the content of Mo oxides at grain boundaries while inhibiting migration of grain boundaries and dislocations, and plays a role in purifying grain boundaries.

(2) Nb can be dissolved in the matrix to realize solid solution strengthening. The average micro-hardness in the FZ is improved from HV 194.7 to HV 283.3, indicating a significant solid solution effect. The average grain sizes of LW joint and

LW-Nb joint are separately 36.5 and 35.2 μm, which indicates that the grain refinement effect is insignificant.

(3) After Nb alloying, the number of LAGBs in the bearing area of the joint increases obviously. From the perspective of the type of grain boundaries and interfacial energy, Nb alloying can strengthen grain boundaries and improve the strength of joints.

(4) The addition of Nb reduces both the number (from 668 to 600) and size (from 756 to 522 μm) of pore defects, albeit without significantly affecting their distribution. Moreover, there is a decrease in the oxygen content observed within these pore defects in Nb-alloyed joints. Overall, Nb alloying contributes to the partial suppression of pore defects.

(5) Compared with LW joint, the tensile strength of LW-Nb joints is improved by 69%, increasing from 327.5 to 551.7 MPa. Nb alloying significantly enhances the strength of the joints, resulting in a change in the fracture mode from intergranular fracture to transgranular cleavage fracture.

## CRediT authorship contribution statement

**Jia-xuan ZHAO:** Conceptualization, Data curation, Investigation, Writing − Original draft, Review & editing; **Hong-da ZHANG:** Investigation, Writing − Review & editing; **Lin-jie ZHANG:** Validation, Investigation, Methodology, Writing − Review & editing; **Xiang-dong DING:** Validation, Methodology, Supervision, Project administration, Funding acquisition; **Yuan-jun SUN:** Investigation, Methodology, Resources; **Guang SUN:** Theoretical guidance, Methodology, Validation.

## Declaration of competing interest

The authors declare that they have no known competing financial interests or personal relationships that could have appeared to influence the work reported in this paper.

## Acknowledgments

This work was supported by the National Key Research and Development Project of China (No. 2022YFB3707602), and the National Natural Science Foundation of China (Nos. 52005393, 51775416). Thanks to the teachers in the Analysis and Test Center of Xi'an Jiaotong University for their help in the experiment in this paper.

## References

[1] GIBSON M, SCHMITZ P. Higher power design concepts for NASA's kilopower reactor [C]//Proceedings of the 2020 IEEE Aerospace Conference. Big Sky, MT, USA: IEEE, 2020: 1−9. https://dx. doi.org/10.1109/AERO47225.2020.9172530.

[2] LIU Ye, ZHOU Lei, ZAN Yuan-feng, HUANG Yan-ping. Review of heat pipe application in advanced nuclear reactors [J]. Nuclear Power Engineering, 2016, 37(6): 121−124. https://dx.doi.org/10.13832/j.jnpe.2016.06.0121. (in Chinese)

[3] LI Jing-wang, DAI Shu-gang. Recent progress and prospect of high temperature heat pipes technology [J]. Chinese Space Science and Technology, 2019, 39(3): 30−42. https://dx.doi.org/10.16708/j.cnki.1000-758X.2019.0018. (in Chinese)

[4] LI Yi, YANG Hui-long, SU Ran-ran, LIU Tong. High-temperature oxidation behavior and degradation mechanism of chromium-coated zirconium alloy cladding: a review [J]. Tungsten, 2025, 7(1): 50-70. https://doi.org/10.1007/s42864-024-00289-7

[5] LI Bo, YANG Hui-long, HOLMES R, CUI Li-juan, KANO S, ABE H. Thermal stability of the Cr-coated zirconium alloy microstructure prepared by pulsed laser deposition [J]. Tungsten, 2024, 6(2): 333-341. https://doi.org/10.1007/s42864-023-00235-z

[6] EL-GENK M S, TOURNIER J M. A review of refractory metal alloys and mechanically alloyed-oxide dispersion strengthened steels for space nuclear power systems [J]. Journal of Nuclear Materials, 2005, 340(1): 93−112. https://dx.doi.org/10.1016/j.jnucmat.2004.10.118.

[7] XU Liu-jie, SUN Tie-long, ZHOU Yu-cheng, LI Zhou, WEI Shi-zhong. Evaluation of tensile property and strengthening mechanism of molybdenum alloy bars doped with different ultrafine oxides [J]. Transactions of Nonferrous Metals Society of China, 2023, 33(10): 3083−3099. https://doi.org/10. 1016/S1003-6326(23)66319-8.

[8] XIE Miao-xia, LI Yan-xin, SHANG Xiang-tao, WANG Xue-wu, PEI Jun-yu. Effect of heat input on porosity defects in a fiber laser welded socket-joint made of powder metallurgy molybdenum alloy [J]. Materials, 2019, 12(9): E1433. https://dx.doi.org/10.3390/ma12091433.

[9] TAO Tao, LIU Jin-shui, ZHOU Dian-wu, LI Hui-ming, WANG Xin-yu. Microstructure and properties of magnesium/steel dissimilar metals by interlayer assisted laser welding [J]. Transactions of Nonferrous Metals Society of China, 2023, 33(3): 765−776. https://doi.org/10.1016/S1003-6326(23)66144-8.

[10] LIU Peng, FENG Ke-yun, ZHANG Ge-ming. A novel study on laser lap welding of refractory alloy 50Mo−50Re of small- scale thin sheet [J]. Vacuum, 2017, 136: 10−13. https://dx. doi.org/10.1016/j.vacuum.2016.11.001.

[11] ZHANG Liang-liang, ZHANG Lin-jie, YANG Qing-jie. Weldability of molybdenum−rhenium alloy based on a single-mode fiber laser [J]. Metals, 2022, 12(5): 841. https://dx.doi.org/10.3390/met12050841.

[12] AN Geng, SUN Jun, SUN Yuan-jun, CAO Wei-cheng, ZHU Qi, BAI Qing-lin, ZHANG Lin-jie. Fiber laser welding of

fuel cladding and end plug made of $La_2O_3$ dispersion-strengthened molybdenum alloy [J]. Materials, 2018, 11(7): 1071. https://dx.doi.org/10.3390/ma11071071.

[13] ZHANG Lin-jie, LIU Jiang-zhe, BAI Qing-lin, WANG Xue-wu, SUN Yuan-jun, LI Si-guang, GONG Xing. Effect of preheating on the microstructure and properties of fiber laser welded girth joint of thin-walled nanostructured Mo alloy [J]. International Journal of Refractory Metals and Hard Materials, 2019, 78: 219−227. https://dx.doi.org/10.1016/j.ijrmhm.2018.10.002.

[14] ZHANG Lin-jie, LIU Jiang-zhe, PEI Jun-yu, NING Jie, ZHANG Liang-liang, LONG Jian, ZHANG Gui-feng, ZHANG Jian-xun, NA S J. Effects of power modulation, multipass remelting and Zr addition upon porosity defects in laser seal welding of end plug to thin-walled molybdenum alloy [J]. Journal of Manufacturing Processes, 2019, 41: 197−207. https://dx.doi.org/10.1016/j.jmapro.2019.04.001.

[15] CHENG Pei-xin, ZHANG Lin-jie, NING Jie, NA S J, PANG Yong-qing. Effects of addition of titanium on microstructures and properties of laser butt welded joints of Mo−30W alloy [J]. Journal of Materials Engineering and Performance, 2022, 31(10): 8542−8553. https://dx.doi.org/10.1007/s11665-022-06863-9.

[16] ZHANG Yong-yun, WANG Ting, JIANG Si-yuan, ZHANG Bing-gang, WANG Yong, FENG Ji-cai. Effect of rhenium content on microstructures and mechanical properties of electron beam welded TZM alloy joints [J]. Journal of Manufacturing Processes, 2018, 32: 337−343. https://dx.doi.org/10.1016/j.jmapro.2018.03.008.

[17] ZHANG Yong-yun, WANG Ting, JIANG Si-yuan, ZHANG Bing-gang, WANG Yong, FENG Ji-cai. Microstructure evolution and embrittlement of electron beam welded TZM alloy joint [J]. Materials Science and Engineering: A, 2017, 700: 512−518. https://dx.doi.org/10.1016/j.msea.2017.05.076.

[18] REN Su-zhen, WANG Xu-zhen, SHI Wei. Physical chemistry [M]. 4th ed. Shanghai: Shanghai Scientific and Technical Publishers, 2013. (in Chinese)

[19] YU Han, ZHANG Hong-da, ZHANG Lin-jie, NING Jie, AN Geng, ZHANG Liang-liang. Regulation of performance of laser-welded socket joint of Mo−14Re ultra-high-temperature heat pipe by introducing Ti into both weld and heat affected zone [J]. Journal of Materials Research and Technology, 2023, 22: 569−584. https://dx.doi.org/10.1016/j.jmrt.2022.11.162.

[20] ZHANG Lin-jie, PEI Jun-yu, ZHANG Liang-liang, LONG Jian, ZHANG Jian-xun, NA S J. Laser seal welding of end plug to thin-walled nanostructured high-strength molybdenum alloy cladding with a zirconium interlayer [J]. Journal of Materials Processing Technology, 2019, 267: 338−347. https://dx.doi.org/10.1016/j.jmatprotec.2018.12.028.

[21] ZHANG Liang-liang, ZHANG Lin-jie, LONG Jian, NING Jie, ZHANG Jian-xun, NA S J. Effects of titanium on grain boundary strength in molybdenum laser weld bead and formation and strengthening mechanisms of brazing layer[J]. Materials & Design, 2019, 169: 107681. https://dx.doi.org/10.1016/j.matdes.2019.107681.

# 超高温钼热管套接接头的铌合金化激光焊接

赵佳璇[1]，张洪达[1]，张林杰[1]，丁向东[1]，孙院军[1]，孙 广[2]

1. 西安交通大学 金属材料强度国家重点实验室，西安 710049；
2. 中国广核集团有限公司，深圳 518172

**摘 要：**研究 Nb 合金化对激光焊接钼套接接头显微组织和性能的影响。Nb 合金化后，焊缝区(FZ)的平均显微硬度由 HV 194.7 提高到 HV 283.3。Nb 与 O 结合形成 $Nb_2O_5$, $Nb_2O_5$ 分散在晶界上，从而阻碍了晶界迁移和位错运动，并降低了晶界处挥发性 Mo 氧化物的含量。在 FZ 中加入 Nb 在一定程度上抑制了孔隙缺陷的危害，提高了接头的承载能力。与未添加 Nb 的接头 (LW)相比，添加 Nb 合金的激光焊接接头(LW-Nb)的抗拉强度从 327.5 MPa 提高到 551.7 MPa，提高了约 69%。此外，接头断裂机理由沿晶断裂转变为穿晶断裂。

**关键词：**激光焊接；钼；热管；铌合金化；显微组织；性能

**(Edited by Wei-ping CHEN)**